Computational Studies of the Farnesyltransferase Ternary Complex Part I: Substrate Binding†

Guanglei Cui, Bing Wang, and Kenneth M. Merz, Jr.*

Department of Chemistry, 104 Chemistry Building, The Pennsylvania State University, University Park, Pennsylvania 16802

Received May 30, 2005; Revised Manuscript Received September 20, 2005

ABSTRACT: Farnesyltransferase (FTase) catalyzes the transfer of farnesyl from farnesyl diphosphate (FPP) to cysteine residues at or near the C-terminus of protein acceptors with a CaaX motif (a, aliphatic; X, Met). Farnesylation is a critical modification to many switch proteins involved in the extracellular signal transduction pathway, which facilitates their fixation on the cell membrane where the extracellular signal is processed. The malfunction caused by mutations in these proteins often causes uncontrolled cell reproduction and leads to tumor formation. FTase inhibitors have been extensively studied as potential anticancer agents in recent years, several of which have advanced to different phases of clinical trials. However, the mechanism of this biologically important enzyme has not been firmly established. Understanding how FTase recruits the FPP substrate is the first and foremost step toward further mechanistic investigations and the design of effective FTase inhibitors. Molecular dynamic simulations were carried out on the ternary structure of FTase complexed with the FPP substrate and an acetyl-capped tetrapeptide (acetyl-CVIM), which revealed that the FPP substrate maintains an inactive conformation and the binding of the diphosphate group can be largely attributed to residues R291β, K164α, K294β, and H248β. The FPP substrate assumes an extended conformation in the binding site with restricted rotation of the backbone dihedral angles; however, it does not have a well-defined conformation when unbound in solution. This is evident from multinanosecond MD simulations of the FPP substrate in a vacuum and solution. Our conclusion is further supported by theoretical *J* coupling calculations. Our results on the FPP binding are in good agreement with previous experimental kinetic studies on FTase mutants. The hypothetical conformational activation of the FPP substrate is currently under investigation.

Farnesyltransferase (FTase) is a zinc metalloenzyme that removes the diphosphate group from the farnesyl diphosphate (FPP) substrate and connects the resulting farnesyl moiety, a 15-carbon isoprenoid, to the cysteine at or near the C-terminus of protein acceptors (Figure 1) (*1*). This post-translational modification is important for many GTP-binding switch proteins on RTK (receptor tyrosine kinase) signal transduction pathways, facilitating their attachment and localization to the inner side of the plasma membrane (*2*−*7*). These proteins function as molecular switches, regulating cell proliferation and differentiation, promoting cell survival, and modulating cellular metabolism. Their malfunction is often associated with uncontrolled cell growth that may lead to tumor and cancer formation. As a member of the GTPase switch protein superfamily, *Ras* is found to be related to roughly 30% of human cancers as a single mutation traps it in the GTP-bound activated state, signaling cell growth even in the absence of growth factors. Interference of the association of these proteins to the plasma membrane through FTase inhibition nearly reduces or terminates the growth of cancer cells, which identifies farnesyltransferase as a viable therapeutic target (*8*−*12*). Several FTase inhibitors (FTIs) have entered different clinical trial phases along the drug discovery pipeline, showing promise in the clinical treatment of human cancers (*13*−*18*).

Through an elucidation of the exact mechanism of farnesylation by FTase the rational design of small molecule therapeutics can be significantly accelerated. Given the importance of FTase, it is not surprising that this protein has been extensively studied by X-ray crystallography (*19*−*25*), steady-state kinetics (*26*, *27*), transient kinetics (*28*), and site-directed mutagenesis (*27*) over the past 10 years. From these studies an overall mechanistic "picture" has been established. Four distinct stages have been identified (Figure 2), including the orderly binding of the FPP substrate and protein targets, the activation of the initial ternary complex that features a 7 Å gap between the two reacting species, the zinc-catalyzed chemical reaction step, which can be accelerated by 700-fold if magnesium ion is present in the binding site, and the rate-limiting product release step. Although the understanding of the farnesylation mechanism has been significantly advanced, many key questions remain unanswered (*29*), most notably the conformational activation of the bound FPP substrate, the binding of a cocatalytic magnesium ion and its function, and the release of farnesylated protein substrates and the biological role of an "exit groove" found in a recently published X-ray structure (*19*). We have embarked on a series of computational studies with the intention of providing valuable insights into these critical issues, starting with the investigation of

† This work was supported by a NIH grant (GM44974) to K.M.M.

* To whom correspondence should be addressed. Telephone: (814) 865-3623. Fax: (814) 865-3292. E-mail: merz@psu.edu.

10.1021/bi051020m CCC: $30.25
Published on Web 11/24/2005

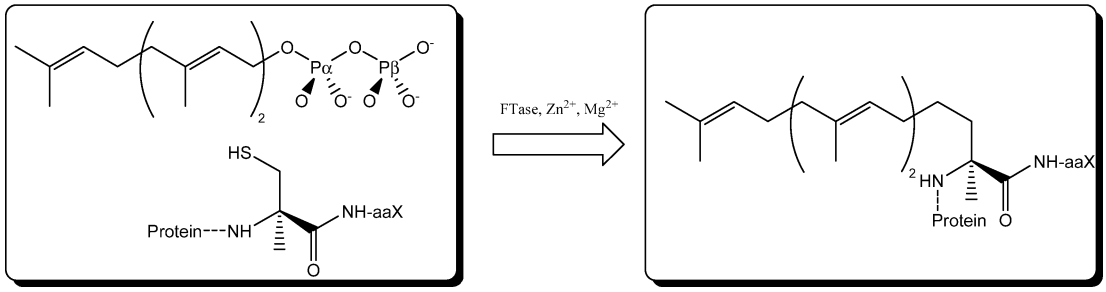

FIGURE 1: The farnesylation reaction.

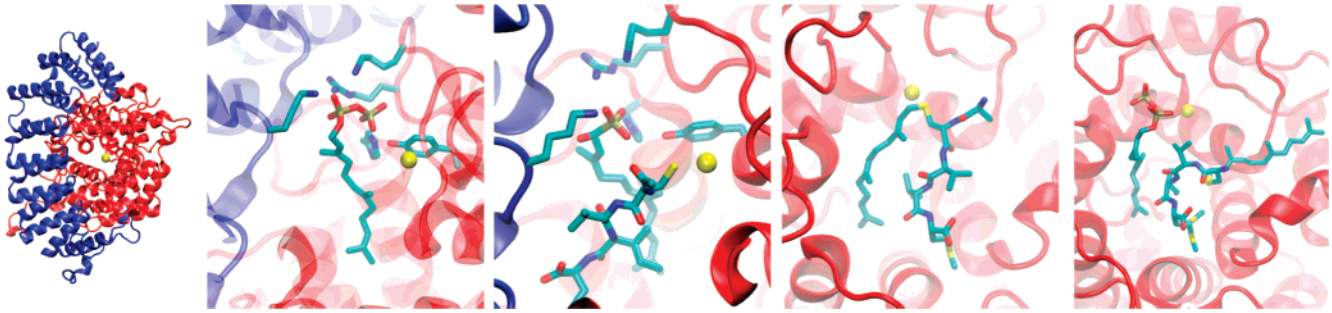

FIGURE 2: Structural evidence that highlights the key waypoints on the farnesylation reaction pathway (from left to right: apo-Ftase, 1FT1; the binary complex of FTase and FPP, 1FT2; the ternary complex of FTase, HFP, and acetyl-CVIM, 1QBQ; product complexes of FTase with the farnesylated peptide, 1KZP and 1KZO).

the FPP substrate binding in the reactive FTase ternary complex.

The binding of the FPP substrate takes place first, followed by the binding of the protein target (*30*, *31*). Studies on FTase mutants suggest that several polar amino acid side chains (K164α, H248*β*, R291*β*, K294*β*, and Y300*β*) contribute to the binding of the FPP substrate; however, the specific interaction between these side chains and the two phosphate groups and the exact location where the interaction is made can only be speculated owing to the lack of structural information of reactive FTase ternary complexes. Several crystal structures of FTase ternary complexes have been solved so far with either FPP analogues or slow peptide substrates or peptide-like inhibitors, and none assumes the postulated active FPP conformation that features a reduced distance between the two reacting species. The crystal structure (PDB code: 1QBQ) of the ternary complex of FTase, α-hydroxyfarnesylphosphonic acid (HFP), and a tetrapeptide (ACE^1-Cys^2-Val^3-Ile^4-MSE^5) indicates that the farnesyl moiety and the tetrapeptide share the same binding site surrounded with hydrophobic residues. Moreover, the side chain of Ile^4 forms close van der Waals contacts with the second isoprene of the farnesyl group. The phosphonic acid moiety of HFP is tightly bound to a highly positively charged pocket, comprising K164α, R291*β*, and K294*β*. In the crystal structure of FTase and FPP binary complex (PDB code: 1FT2), H248*β* and Y300*β* are also involved in FPP binding by hydrogen bonding to the *β*-phosphate. Mutations of these amino acid side chains cause the decrease in the rate of chemistry (k_{chem}) measured from steady-state kinetics experiments, which leads to the proposal of a general acid−base mechanism with Y300*β* and K164α serving as the catalytic residues (*27*, *32*). However, the functions of these conserved amino acid residues in the enzymatic reaction were reexamined in a recent transient kinetics study (*28*), which argued that Y300*β*, H248*β*, and K164α mainly stabilize and position the diphosphate moiety into a "pose" that is suitable for the following chemical reaction. To design effective FTase inhibitors that compete with FPP binding, accurate and consistent structural and dynamic information of the FPP binding site is of great value.

Obtaining this information based solely on X-ray crystallography and biochemical/biophysical assays can be difficult, but they offer an excellent starting point for theoretical studies. Here we provide insights into FPP binding, particularly the functions of residues K162α, R291*β*, K294*β*, H248*β* ,and Y300*β*, with detailed structural and dynamic information of the FTase ternary complex with FPP and a reactive tetrapeptide substrate (acetyl-CVIM) from a 5.8 ns molecular dynamics (MD) simulation. To our knowledge, this is the first MD simulation of FTase and substrate complexes reported so far. Previously, only the zinc-bound FTase was studied with a 1 ns molecular dynamics simulation (*33*), in which the zinc site was modeled with the cationic dummy atom approach, suggesting relatively large conformational flexibility of nine conserved residues in the FTase active site. In our study, we focus on the specific binding of the FPP diphosphate group and the conformational preference of the bound farnesyl group. The bonded approach of Hoops et al. was used (*34*), in which harmonic covalent bonds were placed between the bound zinc and the four surrounding first-shell amino acid side chains.

Molecular dynamics simulation has the advantage of studying largely experimentally inaccessible states, giving us the opportunity to directly examine the key elements in FPP binding. Farnesyl diphosphate is tightly bound in the hydrogen bond network formed by residues K164α, R291*β*, K294*β*, and H248*β*. The interactions of these residues with the two phosphate units are analyzed in detail below. Qualitatively, our findings from the 5.8 ns MD simulation, particularly the specific interactions between the two phosphate groups and FPP binding residues, are in excellent agreement with what have been reported from transient kinetics studies (*28*). The FTase ternary complex remains

in the inactive conformation with the two participating "reactive" atoms of farnesylation remaining separated by over 7 Å. Our analysis demonstrates that Y300β is too distant to make a significant contribution to the binding of the FPP substrate. It is known that the mutation of residue Y300β decreases the reaction rate by almost 500-fold. We speculate that it may promote the reaction rate by assisting FPP in its approach toward the nucleophile or by stabilizing the leaving diphosphate group. The definitive role of residue Y300β will be left for future work. In the following sections, we focus on the description of our simulation methods of the FTase ternary complex and present a detailed analysis of our results.

METHODS

The model structure of FTase and the substrates forming the ternary complex were built from two crystal structures (PDB codes: 1FT2 and 1QBQ). 1FT2 is the binary complex of FTase and FPP, while 1QBQ is the ternary complex of FTase, the peptide substrate (acetyl-CVIM), and HFP. Both structures were solved at resolutions of above 2 Å (*23*). The backbone conformations defined by the atoms C, CA, N, and O were almost unaltered upon the binding of the peptide substrate (root mean square deviation is 0.8 Å). The two superimposed structures were then merged to give the structure of the reactive FTase ternary complex with HFP replaced by FPP from X-ray structure 1FT2. The FPP binding site is sandwiched between two FTase subunits, fully accessible to solvent. Ten crystal water molecules were found within 5 Å of HFP in the X-ray structure 1QBQ. Ionizable amino acid side chains (Asp, Glu, Arg, and Lys) in the FPP binding site were modeled in their usual protonation states corresponding to physiological pH, and FPP was fully deprotonated, bearing three negative charges. The 25 histidine residues found in 1QBQ were all treated as neutral. Moreover, via visual inspection, the protonation pattern was selected on the basis of the formation of reasonable hydrogen-bonding networks between the His residues and its surrounding environment. The cysteine of the zinc-bound peptide was modeled as a thiolate, which is the more widely accepted protonation state for this residue, although the possibility of having a zinc-bound thiol form of the peptide cannot be ruled out entirely (*29*). A total of 284 crystallographically determined solvent molecules from 1QBQ were carried into the final structure. All molecular mechanics (MM) and dynamics simulations were conducted with the *sander* module in the AMBER8 modeling suite (*35*). Cornell's *ff94* force field for proteins (*36*) and Wang's *gaff* force field for small organic compounds (*37*) were used in the simulation with missing force field parameters developed using protocols described below. Quantum mechanics (QM) calculations needed during the parametrization process were carried out with Gaussian'98 (*38*) and Gaussian'03 (*39*). In general, missing partial charges were derived following a two-stage restrained electrostatic potential (RESP) fitting procedure (*40*, *41*) after geometry optimization at HF/6-31G*. The energy profiles for unknown dihedral angle types were obtained by taking the difference of computed quantum mechanics and molecular mechanics energies ($E_{QM} - E_{MM}$) of a set of QM optimized conformations with preassigned dihedral angles (*36*). This energy profile was then least-squares fitted with a sum of cosine terms by varying the magnitude, phase, and multiplicity of each term.

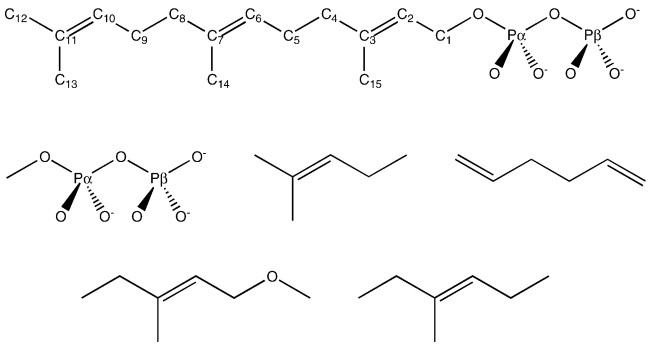

FIGURE 3: Farnesyl diphosphate and model compounds used in force field parameter development.

Parametrization of the Zinc Environment. The bonded approach was employed to model the zinc−ligand interactions in the molecular mechanics treatment (*34*, *42*). It has been shown in our previous studies (*43*−*45*) that the bonded approach is a straightforward and effective way to retain the tetrahedral geometry of the zinc−ligand coordination environment and the electrostatic characteristics of the zinc−ligand interactions. The force field parameters needed to model the zinc environment in the protein were derived from a truncated cluster model, in which each ligating amino acid was represented only by its side chain atoms. The zinc ion in the FTase ternary complex is coordinated by four amino acids, Asp297β, Cys299β, His362β, and Cys1*p* from the peptide substrate, which was then represented as [Zn−(methylthiolate)$_2$(methylimidazole)(acetate)]$^{-1}$ in our cluster model.

Starting with the geometry in the crystal structure, this cluster model was optimized with QM in a vacuum using B3LYP/6-31 + G*. The zinc−ligand covalent bond parameters and atomic charges were then derived using the optimized geometry following protocols described in detail elsewhere (*43*−*45*). The new atomic charges were then incorporated with the atomic charges in *ff94* while keeping the atomic charges of the backbone atoms intact. The equilibrium values for the added bond lengths and bond angles were taken from the X-ray crystal conformation. All of the parameters used to represent the zinc environment in the FTase ternary complex are included in the Supporting Information.

Parametrization of Farnesyl Diphosphate. Farnesyl diphosphate is a 49-atom molecule that can be divided into three isoprenoid groups and one diphosphate group. Crystallographic evidence reveals that FPP is initially locked in an inactive conformation by FPP binding residues (possibly a combination of K164α, R291β, K294β, H248β, and Y300β), which creates a 7.2 Å gap between the two reacting centers. On the basis of the comparison of the FPP conformations in 1QBQ and the FTase product complex (PDB code: 1KZP), it has been hypothesized that rotation of the diphosphate-connecting isoprenoid group eliminates the gap so that the following chemical events can be carried out (*19*). So, it is important to accurately model the conformational preferences of the isoprenoid groups by our classical force field for any of the following simulations to be meaningful. We systematically derived missing force field parameters from quantum mechanical calculations on small fragments (Figure 3). This divide-and-conquer strategy should offer better transferability

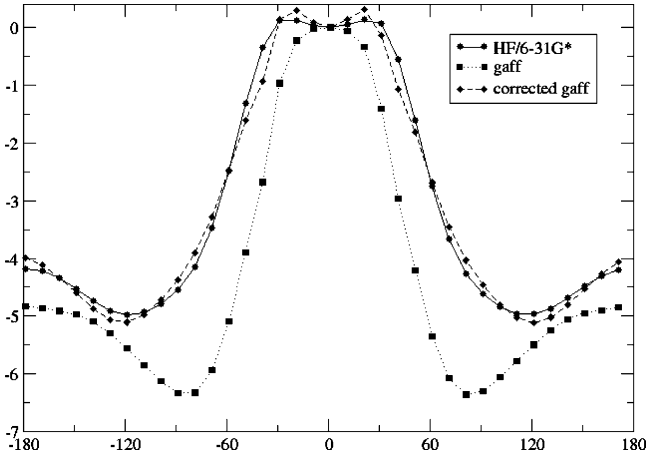

FIGURE 4: Torsion profile for the dihedral of type c2−c2−c3−c3.

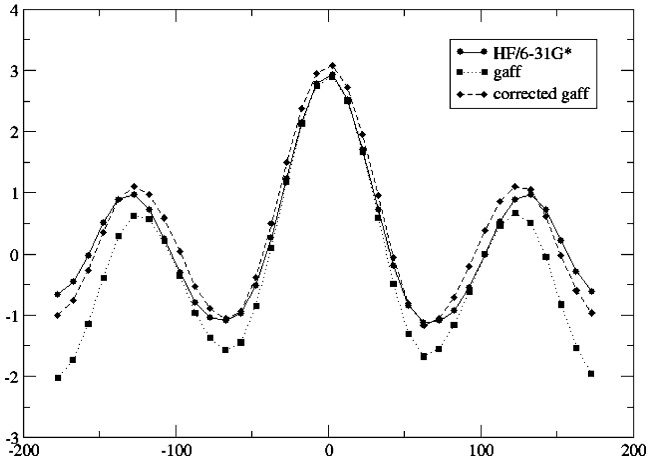

FIGURE 5: Torsion profile for the dihedral of type c3−c3−c2−c3.

and less conformational dependency of the derived parameters (*36*).

gaff, a generic AMBER-compatible force field for small organic compounds, was used as the starting point for the model building process. Proper atom types were conveniently assigned using the *antechamber* module included in the AMBER8 suite of programs. sp^3 and sp^2 carbon atoms were assigned atom type c3 and c2, respectively. Each unique dihedral angle type in the farnesyl group was closely examined to ensure a close agreement between QM and MM calculated torsion profiles evaluated at 36 rotational conformers optimized at the HF/6-31G* level of theory. Energy profiles evaluated with MP2/6-31G* on calculated minima along the rotational angles are in agreement with those calculated with HF/6-31G* (data not shown). Therefore, HF/6-31G* calculated profiles were used to reduce the computational cost. Two new torsion terms for dihedral types c3−c3−c2−c2 and c3−c3−c2−c3 were necessary from the superposition of the QM and MM calculated torsion profiles (see Figures 4−6). The energy minima found on the torsion profiles were also used in multiconformer RESP charge calculations, during which neutrality constraints were applied on capping methyl groups (*41*). Therefore, the net −3 charge of FPP was assigned completely to the diphosphate group. The derived atomic charges and augmented torsion terms can be found in the Supporting Information.

QM J Coupling Calculation of Farnesyl Diphosphate. To determine the conformational preference of FPP, we have

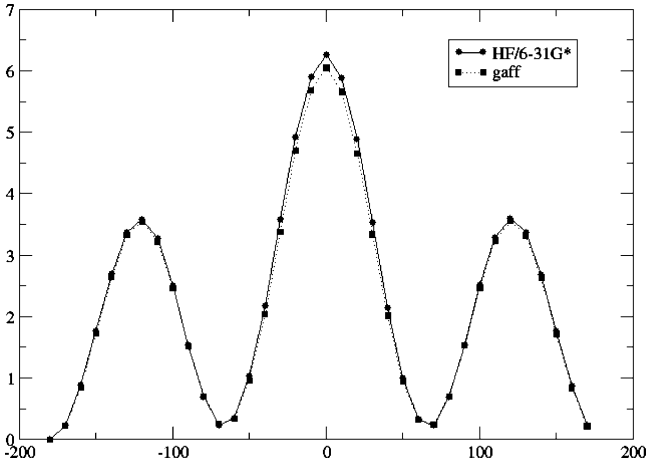

FIGURE 6: Torsion profile for the dihedral of type c2−c3−c3−c2.

carried out *J* coupling constant calculations on the model molecule 1,5-hexadiene. Conformers were generated by the variation of the $\phi 2$ dihedral angle from −180° to 0° in 10° intervals. Geometries of these conformers were optimized at the Hartree−Fock (HF)/6-31G* level. Indirect spin−spin coupling constants were determined at the B3LYP/6-311G** level of theory. All four contributions (Fermi contact, diamagnetic spin−orbital, paramagnetic spin−orbital, spin−dipole) were included in the coupling constant calculations, although the Fermi contact terms were generally found to be dominant.

MD Simulation of the Farnesyltransferase Ternary Complex. The MD simulation of the FTase ternary complex was conducted at 300 K and 1 atm (NPT ensemble). The particle mesh Ewald [PME (*46*)] method was used in the explicit solvent MD simulation of the FTase ternary complex. The default PME parameter values in AMBER were used (8 Å cutoff for the real-space nonbonded interactions and a reciprocal space grid spacing of approximately 1 Å). The net charge of the entire system was −23 and was neutralized by applying a uniform neutralizing plasma (*47*, *48*), which raised every point charge in the system by 0.0003. A net neutral system is a requirement of the Ewald summation method and can also be achieved by adding explicit cations, such as Na^+. Including explicit ions during MD simulations is important in cases where ions are involved in specific interactions with the solute, such as DNA; however, it increases the computational cost due to the relatively long relaxation time of explicit ions. The ternary complex was solvated in an octahedral periodic box with each side at least 8 Å from the closest solute atoms. The three-site constrained water model TIP3P (*49*) was used in the simulation. SHAKE was used to fix the length of covalent bonds in which hydrogen atoms were involved (*50*). Rigid body motion of the system as a whole was removed (*51*). The whole system (67342 atoms) was first relaxed to remove possible steric clashes with several short, weakly restrained, energy minimizations, and then the system temperature was slowly brought up to 300 K over 50 ps of MD simulation with a 1 fs time step. Concomitantly, the restraining force was gradually removed. The whole system was coupled to a temperature bath (coupling strength 1.0 ps) controlled by Berendsen's weak coupling method (*52*). At the end of the relaxation process, various mechanical properties of the system (density, potential energy, and volume) had reached

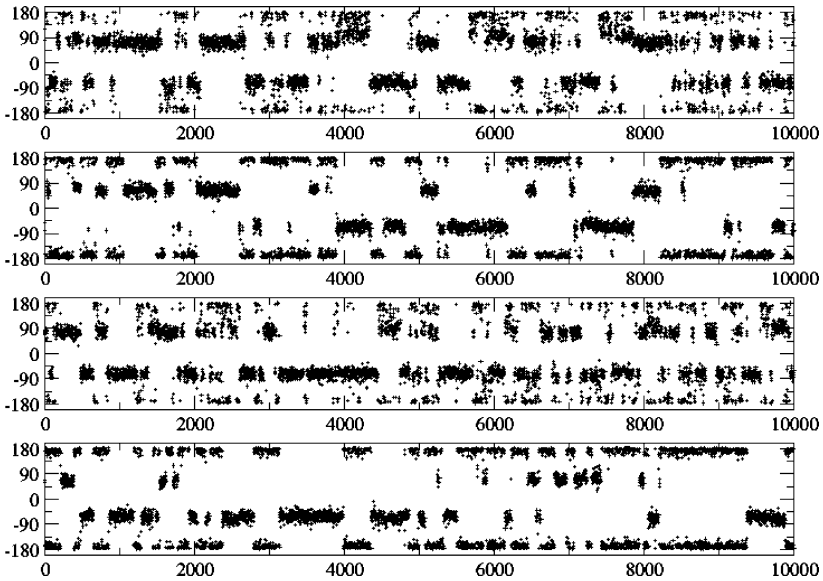

FIGURE 7: FPP backbone dihedral angle distributions in the gas-phase MD simulation (ϕ1, ϕ2, ϕ3, and ϕ4, from top to bottom).

stable values. The production portion of the MD simulation was then carried out for 5.8 ns with a 2 fs time step. During the simulation, snapshots were saved every 2 ps.

Potential of Mean Force Calculations. The conformational preference of the ϕ2 dihedral angle (defined by C3−C4−C5−C6) of FPP was determined by potential of mean force (PMF) calculations both in a vacuum and in aqueous solution (*53*). The rotation of ϕ2 was sampled via 36 MD simulations using umbrella biasing potentials, which were harmonic functions whose centers were uniformly distributed between −180° and 180°. The same biasing strength [32.4 kcal/(mol·rad^2)] was used for all biased MD simulations, each of which was equilibrated for 1 ns followed by another 1 ns of data collection. The dihedral values sampled were saved every 20 ps, which resulted in 50000 data points for each MD simulation. The weighted histogram method (WHAM) (*54*) was used to reconstruct the unbiased dihedral distribution from the 50000 × 36 dihedral values sampled and to calculate the free energy profile for the rotation around ϕ2. The convergence criterion of the WHAM analysis was 0.001 kcal. A few extra biased MD simulations were carried out to increase the sampling at select points in order to yield smooth free energy profiles. The statistical uncertainty of the calculated free energy profiles was estimated by a Monte Carlo bootstrap analysis.

RESULTS AND DISCUSSION

Conformational Preference of Farnesyl Diphosphate. Previously, both chemical reactivity studies and structural studies suggested that farnesyl diphosphate prefers a self-coiled or folded conformation especially in hydrophilic solvents (*55*−*58*). However, a recent NMR spectroscopic study (*59*) argued, based on the measured *J* coupling constants, that a more extended conformation is dominant regardless of the nature of the surrounding environment, characterized by the trans conformation of the two isoprenoid groups (torsion angles defined by C3−C4−C5−C6, ϕ2, and C7−C8−C9−C10, ϕ4). Our QM calculated torsion profile for dihedral type c2−c3−c3−c2 indicated that both trans and gauche conformations correspond to energy minima with almost equal probability (trans is only favored over gauche by 0.2 kcal/mol; Figure 6). The gauche and trans conformations are predicted to be separated by an energy barrier of 3.5 kcal/mol. Hence, the transition between trans and gauche conformers at room temperature is unlikely to be significantly hindered. We carried out MD simulations of free FPP both in the gas phase and in solution (10 ns each). It is clear from Figure 7 that both trans and gauche conformations were significantly populated in the gas phase. The free energy profiles of the rotation of ϕ2 in the gas phase and the aqueous phase were calculated with umbrella sampling techniques combined with WHAM (Figure 8). The trans populations of ϕ2 calculated from the WHAM analysis in the gas phase and in solution were 52.6% and 59.9%, respectively, which were calculated by integrating the trans and gauche density distributions. The overall characteristics of the calculated free energy profiles closely resemble the potential energy profile calculated by QM. The solvation effect on the rotation of ϕ2 was not substantial. However, solvation did affect the barrier height near 0°, and perhaps more importantly, the population of gauche conformers was reduced by 7.3%. This indicates that a slightly more compact FPP structure was found in the gas phase, which was further confirmed by the radius of gyration (R_g) of FPP in two different environments. On average, FPP is 0.7 Å smaller in the gas phase than in solution. Although somewhat counterintuitive since we expected hydrophobicity-induced intramolecular self-packing in aqueous solution, the favorable electrostatic attraction between the β-phosphate and the sp^2 hydrogen atom in the first isoprenoid group is a major contributor to a more compact structure in the gas phase. In a high dielectric solvent, this electrostatic contact is greatly weakened due to the strong solvation of the diphosphate group.

The *J* coupling constants for ϕ2 were calculated using the model compound 1,5-hexadiene, in the gas phase, at 18 discrete dihedral angles (Figure 10) and were interpolated with cubic spline. The ensemble-averaged *J* coupling constants of ϕ2 in the gas and aqueous phases were found to be 3.6 ± 0.1 and 3.9 ± 0.1, respectively. The gas-phase result is in excellent agreement with the measured *J* coupling constant (3.6 ± 0.2) for [3,6-bis-^{13}C]farnesol in $CDCl_3$ (*60*), while the solution result is higher than that measured

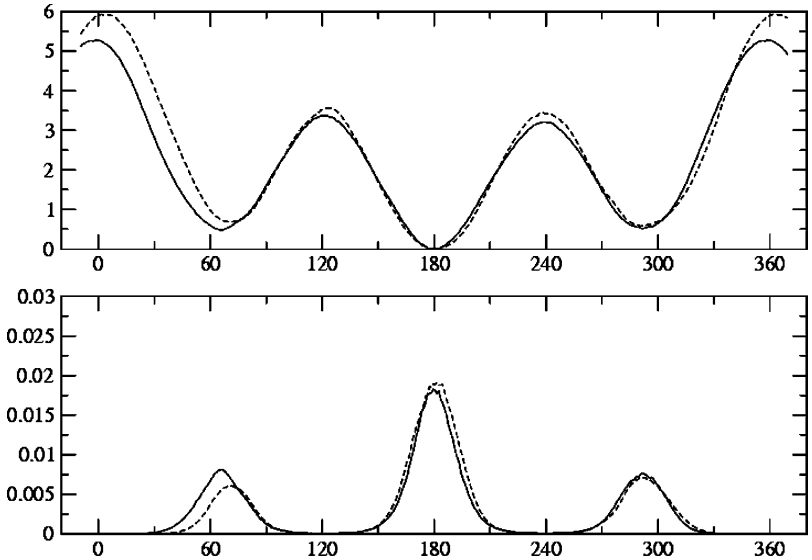

FIGURE 8: Free energy profiles of $\phi 2$ (top, kcal/mol vs deg) in the gas phase (solid line) and in solution (dash line). The corresponding dihedral probability densites were shown at the bottom. The errors in the calculated free energy profiles were not plotted for clarity; in general, the statistic uncertainty at any given point is within ± 0.02 kcal/mol.

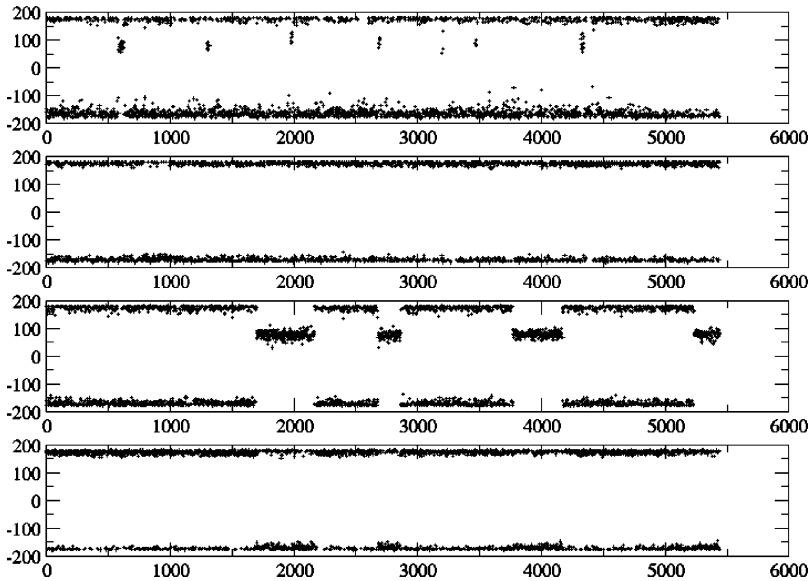

FIGURE 9: FPP backbone dihedral angle distribution in the MD simulation of the FTase ternary complex ($\phi 1$, $\phi 2$, $\phi 3$, and $\phi 4$, from top to bottom).

(3.5 ± 0.2) for [3,6-bis-^{13}C]FPP in D_2O. Nonetheless, we note that both trans and gauche conformations are readily accessible at room temperature, and the dominant conformation of unbound FPP is unlikely to be extended on the basis of our MD simulation results and the calculated ensemble-averaged *J* coupling constants. On the other hand, the transition between trans and gauche is nearly prohibited when FPP is bound (Figure 9). As a matter of fact, the rotations of other farnesyl dihedral angles are frozen as well (data not shown). The extensive van der Waals contacts formed between the farnesyl group and the surrounding FTase and peptide residues, particularly Y166α, R202*β*, G250*β*, Y251*β*, and W303*β*, make other conformations less accessible.

Farnesyltransferase Ternary Complex. The simulated FTase solution structure closely resembles the X-ray crystal structure. The backbone RMSD is around 1.3 Å, and the overall heavy-atom RMSD is 1.8 Å (Figure 11). The crystal geometry of the zinc−ligand coordination environment was well reproduced (Table 1). Although we have not addressed whether the peptide substrate is bound as a thiol or thiolate (an unsolved issue raised in ref *29*), what we were most interested in understanding was the interaction of the FPP diphosphate moiety with its surroundings. Our choice of the protonation state only reflects the tight-binding form (*32*, *61*, *62*) in the most accepted interpretation on this issue, which pictures that the peptide substrate enters the binding site in its thiol form and is subsequently deprotonated by a nearby residue, possibly K164α (*28*).

The two phosphate units of FPP interact mostly with five amino acid side chains, H248*β*, K164α, R291*β*, K294*β*, and Y300*β*, which have been recently probed with transient kinetics experiments (*28*). We have examined the distances of these residues to each individual phosphate unit (P_α and P_β), which qualitatively addresses the strength of the individual interactions. K294*β* is almost equally distant to the two phosphorus atoms (P_α and P_β, Figure 12). The average distance of 3.5 Å suggests strong multiple hydrogen bond interactions with the oxygen atoms on the phosphorus

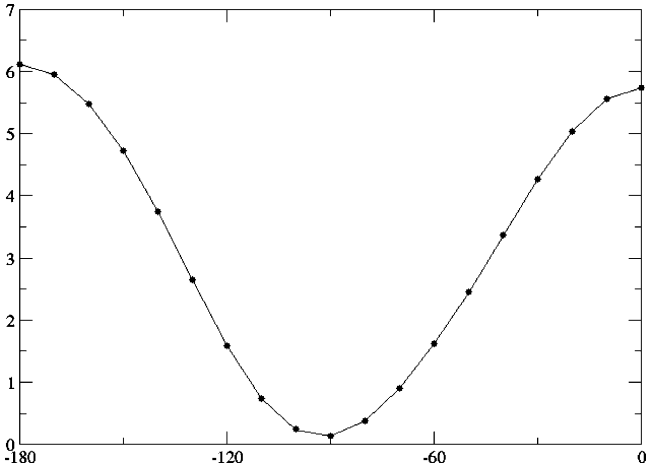

FIGURE 10: *J* coupling constants of dihedral type c2−c3−c3−c2 calculated at 18 discrete dihedral angle values using B3LYP/6-31G* optimized geometries of 1,5-hexadiene.

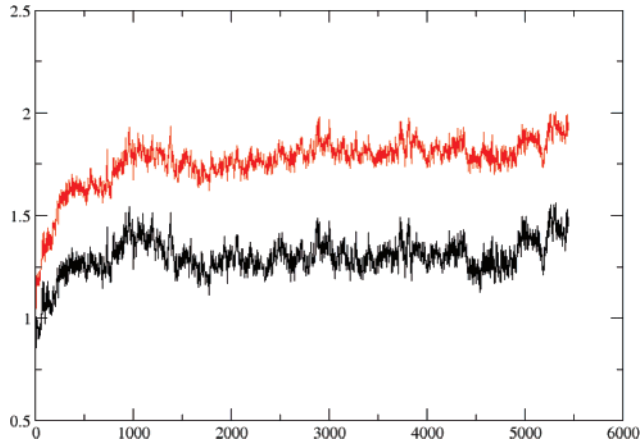

FIGURE 11: Root mean square deviation (in angstroms) of the 5.8 ns MD simulation of the FTase ternary complex (black, backbone atoms only; red, all heavy atoms).

Table 1: Geometry of the Zinc−Ligand Coordination

	crystal value	average from MD
Zn−His362β	2.24	2.22
Zn−Cys299β	2.21	2.20
Zn−Cys1p	2.48	2.46
Zn−Asp297β (OD2)	1.90	1.85
His362β−Zn−Cys299β	121	128
His362β−Zn−Cys1p	97	99
His362β−Zn−Asp297β (OD2)	132	138
Cys299β−Zn−Cys1p	111	96
Cys1p−Zn−Asp297β (OD2)	91	86
Cys299β−Zn−Asp297β (OD2)	100	93

atoms (the average bond length between the phosphorus and nonbridging oxygen atoms was ~1.48 Å). R291β, 5.5 Å from the β-phosphate, primarily interacts with the α-phosphate through bidentate hydrogen bonds involving atom NE and NH2 (Figure 13). The exact hydrogen bond patterns of R291β and K294β slightly differ from what was observed in the FTase ternary complex with FPP and a slow peptide substrate (PDB code: 1JCQ) (*20*), in which the R291βNE hydrogen-bonds to an oxygen atom on the β-phosphate and K294β only interacts with a terminal oxygen atom on the β-phosphate. However, there is little doubt that these two positive residues are deeply involved in FPP binding (Figure 14).

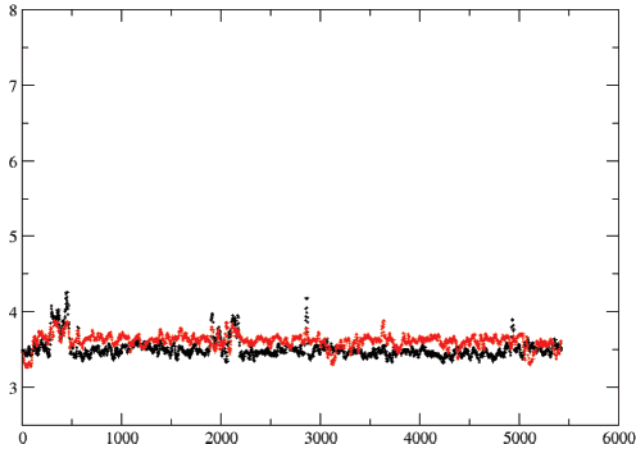

FIGURE 12: Distances from K294NZ to the two diphosphate phosphorus atoms (black, P_α; red, P_β). The distances were averaged every 20 ps.

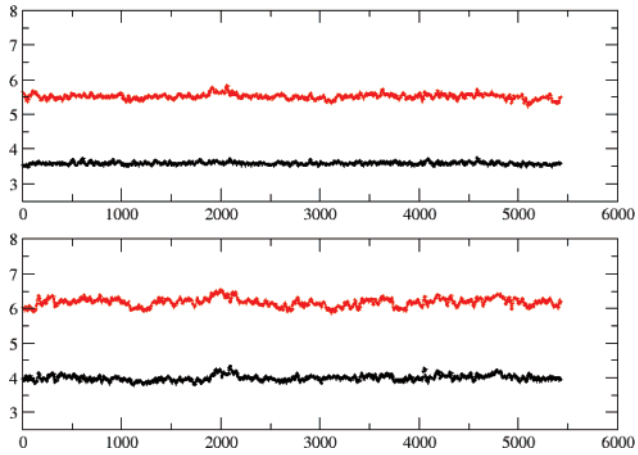

FIGURE 13: Distances from R291βNH2 (top) and R291βNE (bottom) to the two diphosphate phosphorus atoms (black, P_α; red, P_β). The distances were averaged every 20 ps.

On the other hand, the exact binding patterns of K164α, H248β, and Y300β have not been unambiguously identified experimentally, except that it has been shown in site-specific mutagenesis experiments that they make different contributions to FPP binding (*26*, *27*). Removing the hydroxyl group from Y300β decreases the rate of chemistry (k_{chem}) by 500-fold while changing H248β and K164α to Ala reduces k_{chem} by 50-fold. Using farnesyl monophosphate (FMP) as substrate, Pickett et al. (*28*) measured the effects of these three mutations on the reactivity of FTase. When compared to what they found when using FPP as substrate led them to conclude that Y300β energetically stabilizes the "reaction-ready" FPP conformation through hydrogen bonds with the α-phosphate. Their experiments also offered "compelling" evidence that K164α does not interact with the α-phosphate and H248β interacts weakly with the α-phosphate. Our MD simulation shows that H248β is further away from the β-phosphate (Figures 15 and 19). The distance between His248βNE2 and the α-phosphate is on average 4.2 Å, 0.7 Å further than what was found for R291β and K294β. At this distance, it may form transient hydrogen bonds with the bridging oxygen atom O1 between the farnesyl group and the α-phosphate. K164α, on the other hand, binds preferably with the β-phosphate (Figures 16 and 19). Additionally, it forms stable hydrogen bonds with the capping acetyl of the peptide

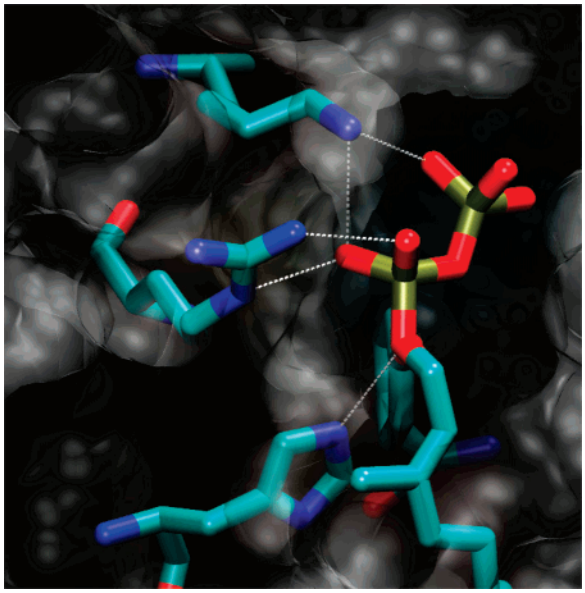

FIGURE 14: Hydrogen bond pattern observed in a snapshot taken at the end of the MD simulation. The highlighted residues are shown as sticks colored by atom names. The rest of the protein is shown as a semitransparent surface colored in gray. The hydrogen bonds that the FPP substrate formed are shown as dotted lines. The residues on the left are K294β, R291β, and H248β. The FPP substrate is overlaid on top of Y300β.

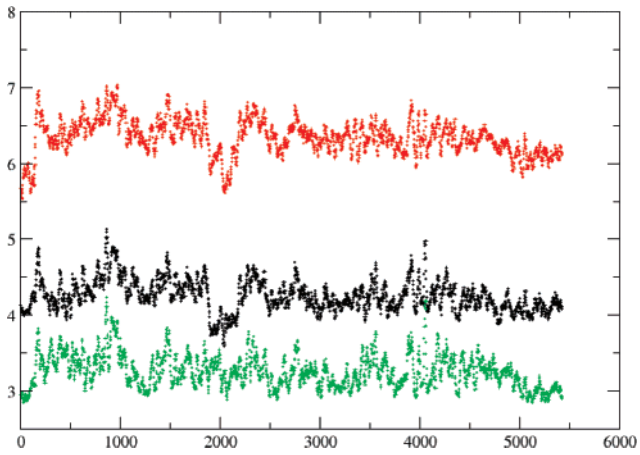

FIGURE 15: Distances from H248β to the two diphosphate phosphorus atoms and the bridging oxygen atom O1 between the farnesyl group and the diphosphate (black, P_α; red, P_β; green, O1). The distances were averaged every 20 ps.

substrate, which is consistent with previous studies that K194α is important for peptide binding (*26*). The close contact of K164α with the backbone carbonyl oxygen of the peptide substrate is also seen in the crystal structure of the FTase ternary complex with the isoprenoid analogue I2 and a K-Ras peptide (*21*). Our simulation suggests that this hydrogen-bonding interaction may not require a protonated peptide substrate, but it could be sequence-dependent.

Mutagenesis experiments established that Y300β is important to farnesylation. Nevertheless, we do not observe Y300β forming any substantial interactions with either of the phosphates (Figures 17 and 19), judging from the distance to either of the diphosphate oxygen atoms. Throughout the 5.8 ns MD simulation, FPP was locked in the "inactive" conformation featuring a large gap between the two reacting

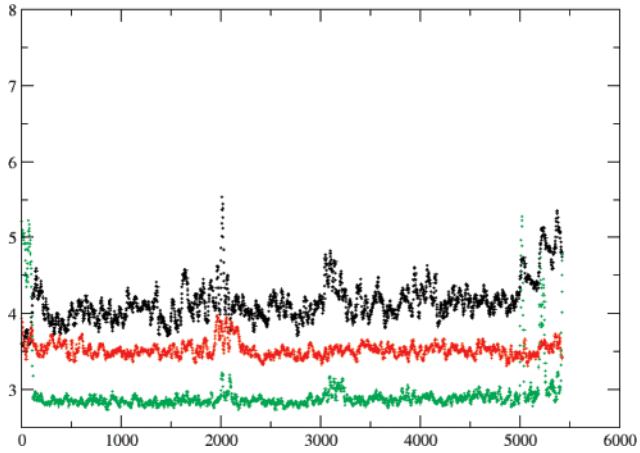

FIGURE 16: Distances from K164β to the two diphosphate phosphorus atoms and the carbonyl oxygen atom (O) at the N-terminus of the peptide substrate (black, P_α; red, P_β; green, O). The distances were averaged every 20 ps.

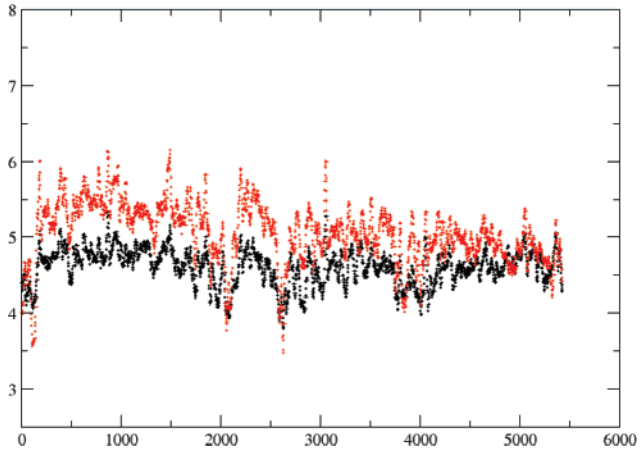

FIGURE 17: Distances from Y300β to the two diphosphate phosphorus atoms (black, P_α; red, P_β). The distances were averaged every 20 ps.

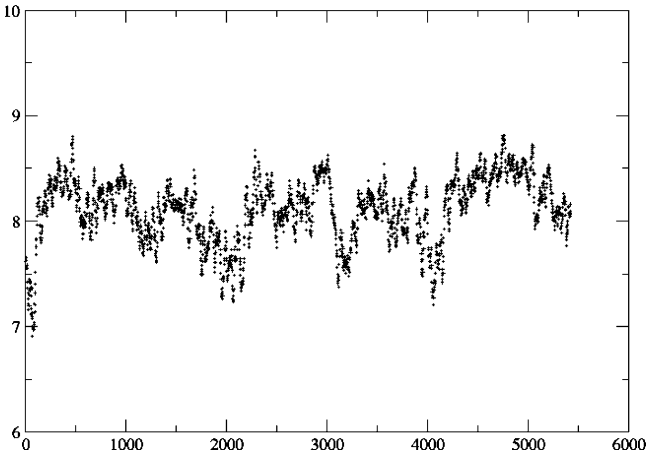

FIGURE 18: Distance between the two reacting centers (C1 of FPP and SG of the peptidic thiolate), averaged every 20 ps.

centers (Figure 18). The time scale of the transition from the inactive conformation to the reaction-ready conformation is likely beyond the reach of standard MD simulation techniques. Although identifying the exact role or roles that Y300β plays requires reaction profile calculations, we agree with the suggestion that Y300β may boost the reaction rate by stabilizing a transitional diphosphate conformation.

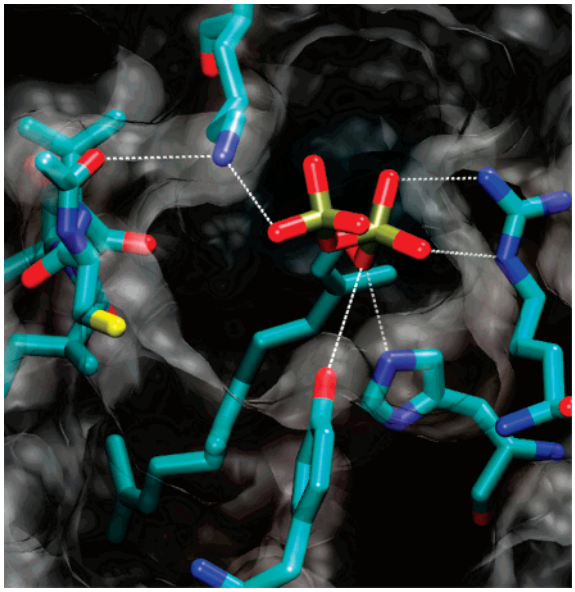

FIGURE 19: Hydrogen bond pattern observed in the same MD snapshot as in Figure 14. R291β and H248β are shown on the right as references points. On the top K164α forms a hydrogen bond with the β-phosphate of the FPP substrate. The tetrapeptide substrate is shown on the left. The hydrogen bond between K164α and the acetyl O was transiently broken near the end of the MD simulation. Y300β is shown at the bottom.

CONCLUSIONS

We have carried out the first molecular dynamics simulation of the farnesyltransferase ternary complex with the two reactive substrates, allowing us to investigate in detail the individual interactions that are crucial to the binding of farnesyl diphosphate. The conformational preference of farnesyl diphosphate was discussed and compared with previous experimental findings. The unbound substrate may adopt either trans or gauche conformations in aqueous solution, but neither appears to be "dominant". The population analysis of multinanosecond MD simulations of the unbound FPP and *J* coupling calculations indicate that FPP is intrinsically flexible and can undergo conformation changes easily in different media. The conformational space of the farnesyl group is significantly reduced upon binding to FTase. The loss of conformational entropy must be compensated by optimal contacts with the hydrophobic residues or side chains in the binding site. The highly negative diphosphate moiety of the FPP substrate is tied to a location that is roughly 8 Å from the peptide binding site. The contribution to binding of the α- and β-phosphate from K164α, R291β, K294β, H248β, and Y300β was qualitatively analyzed and was in good agreement with previous transient kinetics studies. The direct simulation of the conformational activation of FPP is computationally difficult owing to the intricate hydrogen bond network and electrostatic and hydrophobic interactions. Moreover, we found a number of long-lived water molecules sandwiched between FPP and the peptide substrates throughout the entire MD trajectory. In the crystal structure of 1QBQ, three well-defined solvent molecules were found in the same location. Therefore, the FPP diphosphate group is at least partially solvated, which makes the FPP conformational activation process even more interesting.

SUPPORTING INFORMATION AVAILABLE

Force field parameters for the zinc coordination sphere in FTase and the FPP substrate. This material is available free of charge via the Internet at http://pubs.acs.org.

REFERENCES

1. Zhang, F. L., and Casey, P. J. (1996) *Annu. Rev. Biochem. 65*, 241−269.
2. Adjei, A. A. (2001) Blocking oncogenic Ras signaling for cancer therapy, *J. Natl. Cancer Inst. 93*, 1062−1074.
3. Resh, M. (1996) Regulation of cellular signalling by fatty acid acylation and prenylation of signal transduction proteins, *Cell. Signalling 8*, 403−412.
4. Seabra, M. (1998) Membrane association and targeting of prenylated Ras-like GTPases, *Cell. Signalling 10*, 167−172.
5. Sinensky, M. (2000) Recent advances in the study of prenylated proteins, *Biochim. Biophys. Acta 1484*, 93−106.
6. Sinensky, M. (2000) Functional aspects of polyisoprenoid protein substituents: roles in protein-protein interaction and trafficking, *Biochim. Biophys. Acta 1529*, 203−209.
7. Roskoski, R. (2003) Protein prenylation: a pivotal posttranslational process, *Biochem. Biophys. Res. Commun. 303*, 1−7.
8. Rowinsky, E. K., Windle, J. J., and Von Hoff, D. D. (1999) Ras protein farnesyltransferase: A strategic target for anticancer therapeutic development, *J. Clin. Oncol. 17*, 3631−3652.
9. Head, J., and Johnston, S. R. D. (2004) New targets for therapy in breast cancer—Farnesyltransferase inhibitors, *Breast Cancer Res. 6*, 262−268.
10. Bell, I. M. (2004) Inhibitors of farnesyltransferase: A rational approach to cancer chemotherapy?, *J. Med. Chem. 47*, 1869−1878.
11. Sausville, E. A., Elsayed, Y., Monga, M., and Kim, G. (2003) Signal transduction-directed cancer treatments, *Annu. Rev. Pharmacol. Toxicol. 43*, 199−231.
12. Nam, N. H., and Parang, K. (2003) Current targets for anticancer drug discovery, *Curr. Drug Targets 4*, 159−179.
13. Khuri, F. R., Glisson, B. S., Kim, E. S., Statkevich, P., Thall, P. F., Meyers, M. L., Herbst, R. S., Munden, R. F., Tendler, C., Zhu, Y. L., Bangert, S., Thompson, E., Lu, C., Wang, X. M., Shin, D. M., Kies, M. S., Papadimitrakopoulou, V., Fossella, F. V., Kirschmeier, P., Bishop, W. R., and Hong, W. K. (2004) Phase I study of the farnesyltransferase inhibitor lonafarnib with paclitaxel in solid tumors, *Clin. Cancer Res. 10*, 2968−2976.
14. Rao, S., Cunningham, D., de Gramont, A., Scheithauer, W., Smakal, M., Humblet, Y., Kourteva, G., Iveson, T., Andre, T., Dostalova, J., Illes, A., Belly, R., Perez-Ruixo, J. J., Park, Y. C., and Palmer, P. A. (2004) Phase III double-blind placebo-controlled study of farnesyl transferase inhibitor R115777 in patients with refractory advanced colorectal cancer, *J. Clin. Oncol. 22*, 3950−3957.
15. Doll, R. J., Kirschmeier, P., and Bishop, W. R. (2004) Farnesyltransferase inhibitors as anticancer agents: Critical crossroads, *Curr. Opin. Drug Discov. Dev. 7*, 478−486.
16. Taveras, A. G., Kirschmeier, P., and Baum, C. M. (2003) Sch-66336 (Sarasar (R)) and other benzocycloheptapyridyl farnesyl protein transferase inhibitors: Discovery, biology and clinical observations, *Curr. Top. Med. Chem. 3*, 1103−1114.
17. Caponigro, F., Casale, M., and Bryce, J. (2003) Farnesyl transferase inhibitors in clinical development, *Expert Opin. Invest. Drugs 12*, 943−954.
18. Huang, C. Y., and Rokosz, L. (2004) Farnesyltransferase inhibitors: recent advances, *Expert Opin. Therapeutic Patents 14*, 175−186.
19. Long, S. B., Casey, P. J., and Beese, L. S. (2002) Reaction path of protein farnesyltransferase at atomic resolution, *Nature 419*, 645−650.
20. Long, S. B., Hancock, P. J., Kral, A. M., Hellinga, H. W., and Beese, L. S. (2001) The crystal structure of human protein farnesyltransferase reveals the basis for inhibition by CaaX tetrapeptides and their mimetics, *Proc. Natl. Acad. Sci. U.S.A. 98*, 12948−12953.
21. Long, S. B., Casey, P. J., and Beese, L. S. (2000) The basis for K-Ras4B binding specificity to protein farnesyl-transferase revealed by 2 angstrom resolution ternary complex structures, *Structure 8*, 209−222.

22. Strickland, C. L., Windsor, W. T., Syto, R., Wang, L., Bond, R., Wu, Z., Schwartz, J., Le, H. V., Beese, L. S., and Weber, P. C. (1998) Crystal structure of farnesyl protein transferase complexed with a CaaX peptide and farnesyl diphosphate analogue, *Biochemistry 37*, 16601−16611.
23. Long, S. B., Casey, P. J., and Beese, L. S. (1998) Cocrystal structure of protein farnesyltransferase complexed with a farnesyl diphosphate substrate, *Biochemistry 37*, 9612−9618.
24. Dunten, P., Kammlott, U., Crowther, R., Weber, D., Palermo, R., and Birktoft, J. (1998) Protein farnesyltransferase: Structure and implications for substrate binding, *Biochemistry 37*, 7907−7912.
25. Park, H. W., Boduluri, S. R., Moomaw, J. F., Casey, P. J., and Beese, L. S. (1997) Crystal structure of protein farnesyltransferase at 2.25 angstrom resolution, *Science 275*, 1800−1804.
26. Hightower, K. E., De, S., Weinbaum, C., Spence, R. A., and Casey, P. J. (2001) Lysine(164)alpha of protein farnesyltransferase is important for both CaaX substrate binding and catalysis, *Biochem. J. 360*, 625−631.
27. Wu, Z., Demma, M., Strickland, C. L., Radisky, E. S., Poulter, C. D., Le, H. V., and Windsor, W. T. (1999) Farnesyl protein transferase: Identification of K164 alpha and Y300 beta as catalytic residues by mutagenesis and kinetic studies, *Biochemistry 38*, 11239−11249.
28. Pickett, J. S., Bowers, K. E., Hartman, H. L., Fu, H. W., Embry, A. C., Casey, P. J., and Fierke, C. A. (2003) Kinetic studies of protein farnesyltransferase mutants establish active substrate conformation, *Biochemistry 42*, 9741−9748.
29. Sousa, S., Fernandes, P., and Ramos, M. (2005) Unraveling the mechanism of the farnesyltransferase enzyme, *J. Biol. Inorg. Chem. 10*, 3−10.
30. Huang, C. C., Hightower, K. E., and Fierke, C. A. (2000) Mechanistic studies of rat protein farnesyltransferase indicate an associative transition state, *Biochemistry 39*, 2593−2602.
31. Furfine, E. S., Leban, J. J., Landavazo, A., Moomaw, J. F., and Casey, P. J. (1995) Protein farnesyltransferase−Kinetics of farnesyl pyrophosphate binding and product release, *Biochemistry 34*, 6857−6862.
32. Rozema, D. B., and Poulter, C. D. (1999) Yeast protein farnesyltransferase. p*K*(a)s of peptide substrates bound as zinc thiolates, *Biochemistry 38*, 13138−13146.
33. Pang, Y. P., Xu, K., El Yazal, J., and Prendergast, F. G. (2000) Successful molecular dynamics simulation of the zinc-bound farnesyltransferase using the cationic dummy atom approach, *Protein Sci. 9*, 1857−1865.
34. Hoops, S. C., Anderson, K. W., and Merz, K. M. (1991) Force-field design for metalloproteins, *J. Am. Chem. Soc. 113*, 8262−8270.
35. Case, D. A., Darden T. A., Cheatham, T. E., III, Simmerling, C. L., Wang, J., Duke, R. E., Luo, R., Merz, K. M., Wang, B., Pearlman, D. A., Crowley M., Brozell, S., Tsui, V., Gohlke, H., Mongan, J., Hornak, V., Cui, G., Beroza, P., Schafmeister, C., Caldwell, J. W., Ross, W. S., and Kollman, P. A. (2004) AMBER8 Modeling Suite, University of California, San Francisco.
36. Cornell, W. D., Cieplak, P., Bayly, C. I., Gould, I. R., Merz, K. M., Ferguson, D. M., Spellmeyer, D. C., Fox, T., Caldwell, J. W., and Kollman, P. A. (1995) A 2nd generation force-field for the simulation of proteins, nucleic-acids, and organic-molecules, *J. Am. Chem. Soc. 117*, 5179−5197.
37. Wang, J., Wolf, R. M., Caldwell, J. W., Kollman, P. A., and Case, D. A. (2004) Development and testing of a general AMBER force field, *J. Comput. Chem. 25*, 1157−1174.
38. Frisch, M. J., Trucks, G. W., Schlegel, H. B., Scuseria, G. E., Robb, M. A., Cheeseman, J. R., Zakrzewski, V. G., Montgomery, J. A., Jr., Stratmann, R. E., Burant, J. C., Dapprich, S., Millam, J. M., Daniels, A. D., Kudin, K. N., Strain, M. C., Farkas, O., Tomasi, J., Barone, V., Cossi, M., Cammi, R., Mennucci, B., Pomelli, C., Adamo, C., Clifford, S., Ochterski, J., Petersson, G. A., Ayala, P. Y., Cui, Q., Morokuma, K., Malick, D. K., Rabuck, A. D., Raghavachari, K., Foresman, J. B., Cioslowski, J., Ortiz, J. V., Stefanov, B. B., Liu, G., Liashenko, A., Piskorz, P., Komaromi, I., Gomperts, R., Martin, R. L., Fox, D. J., Keith, T., Al-Laham, M. A., Peng, C. Y., Nanayakkara, A., Gonzalez, C., Challacombe, M., Gill, P. M. W., Johnson, B. G., Chen, W., Wong, M. W., Andres, J. L., Head-Gordon, M., Replogle, E. S., and Pople, J. A. **(**1998) *Gaussian 98*, Gaussian, Inc., Pittsburgh, PA.
39. Frisch, M. J., Trucks, G. W., Schlegel, H. B., Scuseria, G. E., Robb, M. A., Cheeseman, J. R., Montgomery, J. A., Jr., Vreven, T., Kudin, K. N., Burant, J. C., Millam, J. M., Iyengar, S. S., Tomasi, J., Barone, V., Mennucci, B., Cossi, M., Scalmani, G., Rega, N., Petersson, G. A., Nakatsuji, H., Hada, M., Ehara, M., Toyota, K., Fukuda, R., Hasegawa, J., Ishida, M., Nakajima, T., Honda, Y., Kitao, O., Nakai, H., Klene, M., Li, X., Knox, J. E., Hratchian, H. P., Cross, J. B., Bakken, V., Adamo, C., Jaramillo, J., Gomperts, R., Stratmann, R. E., Yazyev, O., Austin, A. J., Cammi, R., Pomelli, C., Ochterski, J. W., Ayala, P. Y., Morokuma, K., Voth, G. A., Salvador, P., Dannenberg, J. J., Zakrzewski, V. G., Dapprich, S., Daniels, A. D., Strain, M. C., Farkas, O., Malick, D. K., Rabuck, A. D., Raghavachari, K., Foresman, J. B., Ortiz, J. V., Cui, Q., Baboul, A. G., Clifford, S., Cioslowski, J., Stefanov, B. B., Liu, G., Liashenko, A., Piskorz, P., Komaromi, I., Martin, R. L., Fox, D. J., Keith, T., Al-Laham, M. A., Peng, C. Y., Nanayakkara, A., Challacombe, M., Gill, P. M. W., Johnson, B., Chen, W., Wong, M. W., Gonzalez, C., and Pople, J. A. (2003) *Gaussian 03*, Gaussian, Inc., Pittsburgh, PA.
40. Bayly, C. I., Cieplak, P., Cornell, W. D., and Kollman, P. A. (1993) A well-behaved electrostatic potential based method using charge restraints for deriving atomic charges−the RESP model, *J. Phys. Chem. 97*, 10269−10280.
41. Cieplak, P., Cornell, W. D., Bayly, C., and Kollman, P. A. (1995) Application of the multimolecule and multiconformational RESP methodology to biopolymers−charge derivation for DNA, RNA, and Proteins, *J. Comput. Chem. 16*, 1357−1377.
42. Ryde, U. (1995) Molecular-dynamics simulations of alcohol-dehydrogenase with a 4-coordinate or 5-coordinate catalytic zinc ion, *Proteins: Struct., Funct., Genet. 21*, 40−56.
43. Suarez, D., Diaz, N., and Merz, K. M. (2002) Molecular dynamics simulations of the dinuclear zinc-beta-lactamase from bacteroides fragilis complexed with imipenem, *J. Comput. Chem. 23*, 1587−1600.
44. Suarez, D., and Merz, K. M. (2001) Molecular dynamics simulations of the mononuclear zinc-beta-lactamase from *Bacillus cereus*, *J. Am. Chem. Soc. 123*, 3759−3770.
45. Diaz, N., Suarez, D., and Merz, K. M. (2001) Molecular dynamics simulations of the mononuclear zinc-beta-lactamase from *Bacillus cereus* complexed with benzylpenicillin and a quantum chemical study of the reaction mechanism, *J. Am. Chem. Soc. 123*, 9867−9879.
46. Darden, T., York, D., and Pedersen, L. (1993) Particle mesh Ewald−an N.Log(N) method for Ewald sums in large systems, *J. Chem. Phys. 98*, 10089−10092.
47. Nijboer, B. R. A., and Ruijgrok, T. W. (1988) On the energy per particle in 3-dimensional and two-dimensional Wigner lattices, *J. Stat. Phys. 53*, 361−382.
48. Darden, T., Pearlman, D., and Pedersen, L. G. (1998) Ionic charging free energies: Spherical versus periodic boundary conditions, *J. Chem. Phys. 109*, 10921−10935.
49. Jorgensen, W. L., Chandrasekhar, J., Madura, J. D., Impey, R. W., and Klein, M. L. (1983) *J. Chem. Phys. 79*, 926−935.
50. Allen, M. P., and Tildesley, D. J. (1987) *Computer Simulation of Liquids*, Clarendon Press, Oxford.
51. Harvey, S. C., Tan, R. K. Z., and Cheatham, T. E. (1998) The flying ice cube: Velocity rescaling in molecular dynamics leads to violation of energy equipartition, *J. Comput. Chem. 19*, 726−740.
52. Berendsen, H. J. C., Postma, J. P. M., Vangunsteren, W. F., Dinola, A., and Haak, J. R. (1984) Molecular-dynamics with coupling to an external bath, *J. Chem. Phys. 81*, 3684−3690.
53. Daan Frenkel, B. S. (2002) *Understanding Molecular Simulation: From Algorithms to Applications*, Vol. 1, 2nd ed., Academic Press, New York.
54. Kumar, S., Bouzida, D., Swendsen, R., Kollman, P., and Rosenberg, J. (1992) The weighted histogram analysis method for free-energy calculations on biomolecules. 1. The Method, *J. Comput. Chem. 13*, 1011−1021.
55. Breslow, R. M., and L. M. (1978) *Tetrahedron Lett.*, 887−890.
56. van Tamelen, E. E. (1968) *Acc. Chem. Res. 1*, 111−120.
57. Murgolo, N., Patel, A., Stivala, S., and Wong, T. (1989) The conformation of dolichol, *Biochemistry 28*, 253−260.
58. Di Bernardo, S., Fato, R., Casadio, R., Fariselli, P., and Lenaz, G. (1998) A high diffusion coefficient for coenzyme Q(10) might be related to a folded structure, *FEBS Lett. 426*, 77−80.
59. Zahn, T., Eilers, M., Guo, Z., Ksebati, M., Simon, M., Scholten, J., Smith, S., and Gibbs, R. (2000) Evaluation of isoprenoid conformation in solution and in the active site of protein-farnesyl transferase using carbon-13 labeling in conjunction with solution- and solid-state NMR, *J. Am. Chem. Soc. 122*, 7153−7164.

60. Zahn, T. J., Eilers, M., Guo, Z. M., Ksebati, M. B., Simon, M., Scholten, J. D., Smith, S. O., and Gibbs, R. A. (2000) Evaluation of isoprenoid conformation in solution and in the active site of protein-farnesyl transferase using carbon-13 labeling in conjunction with solution- and solid-state NMR, *J. Am. Chem. Soc. 122*, 7153−7164.
61. Hightower, K. E., Huang, C. C., Casey, P. J., and Fierke, C. A. (1998) H-Ras peptide and protein substrates bind protein farnesyltransferase as an ionized thiolate, *Biochemistry 37*, 15555−15562.
62. Saderholm, M. J., Hightower, K. E., and Fierke, C. A. (2000) Role of metals in the reaction catalyzed by protein farnesyltransferase, *Biochemistry 39*, 12398−12405.

BI051020M